Biomedical Optics EXPRESS

Design and evaluation of a laboratory prototype system for 3D photoacoustic full breast tomography

Wenfeng Xia,[1,*] Daniele Piras,[1] Mithun K. A. Singh,[1] Johan C. G. van Hespen,[1] Ton G. van Leeuwen,[1,2] Wiendelt Steenbergen,[1] and Srirang Manohar[1]

[1]*Biomedical Photonic Imaging group, Mira Institute for Biomedical Technology and Technical Medicine, University of Twente, P.O. Box 217, 7500AE Enschede, The Netherlands.*
[2]*Biomedical Engineering and Physics, Academic Medical Center, University of Amsterdam, P.O. Box 2270, 1100 DE Amsterdam, The Netherlands.*
[*]*W.Xia@utwente.nl*

Abstract: Photoacoustic imaging can visualize vascularization-driven optical absorption contrast with great potential for breast cancer detection and diagnosis. State-of-the-art photoacoustic breast imaging systems are promising but are limited either by only a 2D imaging capability or by an insufficient imaging field-of-view (FOV). We present a laboratory prototype system designed for 3D photoacoustic full breast tomography, and comprehensively characterize it and evaluate its performance in imaging phantoms. The heart of the system is an ultrasound detector array specifically developed for breast imaging and optimized for high sensitivity. Each detector element has an acoustic lens to enlarge the acceptance angle of the large surface area detector elements to ensure a wide system FOV. We characterized the ultrasound detector array performance in terms of frequency response, directional sensitivity, minimum detectable pressure and inter-element electrical and mechanical cross-talk. Further we evaluated the system performance of the laboratory prototype imager using well-defined breast mimicking phantoms. The system possesses a 2 mm XY plane resolution and a 6 mm vertical resolution. A vasculature mimicking object was successfully visualized down to a depth of 40 mm in the breast phantom. Further, tumor mimicking spherical objects with 5 and 10 mm diameter at 20 mm and 40 mm depths are recovered, indicating high system sensitivity. The system has a 170 x 170 x 170 mm^3 FOV, which is well suited for full breast imaging. Various recommendations are provided for performance improvement and to guide this laboratory prototype to a clinical version in future.

OCIS codes: (110.5120) Photoacoustic imaging; (040.0040) Detectors; (170.3830) Mammography; (110.6955) Tomographic imaging.

References and links

1. A. Jemal, F. Bray, M. M. Center, J. Ferlay, E. Ward, and D. Forman, "Global cancer statistics," CA Cancer J. Clin. **61**(2), 69–90 (2011).

#194418 - $15.00 USD Received 25 Jul 2013; revised 10 Sep 2013; accepted 13 Sep 2013; published 23 Oct 2013

2. D. R. Youlden, S. M. Cramb, N. A. M. Dunn, J. M. Muller, C. M. Pyke, and P. D. Baade, "The descriptive epidemiology of female breast cancer: An international comparison of screening, incidence, survival and mortality," Cancer Epidemiology **36**, 237–248 (2012).
3. D. B. Kopans, *Breast Imaging* (Wolters Kluwer Health, 2007)
4. B. Tromberg, B. W. Pogue, K. D. Paulsen, A. G. Yodh, D. A. Boas and A. E. Cerussi, "Assessing the future of diffuse optical imaging technologies for breast cancer management," Med. Phys. **35**, 2443–2451, (2008)
5. C. Lutzweiler, and D. Razansky, "Optoacoustic Imaging and Tomography: Reconstruction Approaches and Outstanding Challenges in Image Performance and Quantification," Sensors **13**(6), 7345–7384, (2013)
6. L. V. Wang and S. Hu, "Photoacoustic tomography: in vivo imaging from organelles to organs", Science **335**,(2012). (doi:10.1126/science.1216210)
7. P. Beard, "Biomedical photoacoustic imaging," Interface Focus **1**, 602–631, (2011)
8. D. Piras, W. Xia, W. Steenbergen, T. G. van Leeuwen and S. Manohar, "Photoacoustic imaging of the breast using the Twente Photoacoustic Mammoscope: Present status and future perspectives," IEEE J. Sel. Topic Quantum. Electron. **16**, 730–739, (2010)
9. R. A. Kruger, R. B. Lam, D. R. Reinecke, S. P. D. Rio and R. P. Doyle, "Photoacoustic angiography of the breast," Med. Phys. **37**, 6096–6100, (2010)
10. S. A. Ermilov, T. Khamapirad, A. Conjusteau, M. H. Leonard, R. Lacewell, K. Mehta, T. Miller and A. A. Oraevsky, "Laser optoacoustic imaging system for detection of breast cancer," J. Biomed. Opt. **14**(2), 024007 (2009)
11. Y. Wang, T. N. Erpelding, L. Jankovic, Z. Guo, J. Robert, G. David and L. V. Wang, "In vivo three-dimensional photoacoustic imaging based on a clinical matrix array ultrasound probe," J. Biomed. Opt. **17**(6), 061208 (2012)
12. F. Ye, S. Yang, and D. Xing, "Three-dimensional photoacoustic imaging system in line confocal mode for breast cancer detection," Appl. Phys. Lett. **97**, 213702 (2010) doi:http://dx.doi.org/10.1063/1.3518704
13. M. Pramanik, G. Ku, C. Li and L. V. Wang, "Design and evaluation of a novel breast cancer detection system combining both thermoacoustic (TA) and photoacoustic (PA) tomography," Med. Phys. **35**, 2218–2223 (2008)
14. M. Heijblom, D. Piras, W. Xia, J.C.G. van Hespen, J.M. Klaase, F.M. van den Engh, T.G. van Leeuwen, W. Steenbergen, and S. Manohar, "Visualizing breast cancer using the Twente photoacoustic mammoscope: What do we learn from twelve new patient measurements?," Opt. Express **20**, 11582–11597 (2012) (doi: http://dx.doi.org/10.1364/OE.20.011582).
15. L. Xi, X. Li, L. Yao, S. Grobmyer, and H. Jiang,"Design and evaluation of a hybrid photoacoustic tomography and diffuse optical tomography system for breast cancer detection," Med. Phys. **39**, 2584-2594 , (2012)
16. V. G. Andreev, A. A. Karabutov and A. A. Oraevsky, "Detection of ultrawide-band ultrasound pulses in optoacoustic tomography," IEEE Trans. Ultrason. Ferr. Freq. Contr. **50**, 1383–1390 (2003).
17. A. Oraevsky, V. G. Andreev, A. A. Karabutov, S. V. Solomatin, E. V. Savateeva, R. D. Fleming, Z. Gatalica, and H. Singh, "Laser optoacoustic imaging of breast cancer in vivo," Proc. SPIE **4256**, 6-15 (2001).
18. R. A. Kruger, K. D. Miller, H. E. Reynolds, W. L. Kiser, D. R. Reinecke and G. A. Kruger, "Breast cancer in vivo: Contrast enhancement with thermoacoustic CT at 434 MHz-feasibility study," Radiology **216**, 279–283 (2000).
19. S. Manohar, A. Kharine, J. C. G. van Hespen, W. Steenbergen, and T. G. van Leeuwen, "Photoacoustic mammography laboratory prototype: Imaging of breast tissue phantoms," J. Biomed. Opt. **9**, 1172–1181 (2004).
20. S. Manohar, S. E. Vaartjes, J. C. G. van Hespen, J. M. Klaase, F. M. van den Engh, W. Steenbergen, and T. G. van Leeuwen, "Initial results of in vivo non-invasive cancer imaging in the human breast using near-infrared photoacoustics," Opt. Express **15**, 12277–12285 (2007).
21. W. Xia, D. Piras, J. C. G. van Hespen, S. van Veldhoven, C. Prins, T. G. van Leeuwen, W. Steenbergen, and S. Manohar,"An optimized ultrasound detector for photoacoustic breast tomography," Med. Phys. **40**(3), 032901 (2013).
22. B. J. Tromberg, N. Shah, R. Lanning, A. Cerrusi, J. Espinoza, T. Pham, L. Svaasand, and J. Butler, "Non invasive *in vivo* characterization of breast tumors using photon migration spectroscopy," Neoplasia **2**, 26–40 (2000).
23. P. Taroni, A. Bassi, D. Comelli, A. Farina, R. Cubeddu, and A. Pifferi, "Diffuse optical spectroscopy of breast tissue extended to 1100 nm," J. Biomed. Opt. **14**, 054030 (1999).
24. W. Xia, D. Piras, J. C. G. van Hespen, W. Steenbergen, and S. Manohar,"A new acoustic lens material for large area detectors in photoacoustic breast tomography," Photoacoustics **1**(2), 9-18 (2013). (doi: http://dx.doi.org/10.1016/j.pacs.2013.05.001)
25. J. Callerama, R. H. Tancrell and D. T. Wilson, "Transmitters and receivers for medical ultrasonics" Ultrasonic Symposium Proceedings, IEEE CH1482-9/79/0000-0407, 407-411, (1979)
26. H. J. Van Staveren, C. J. M. Moes, J. van Marie, S. A. Prahl and M. J. C. van Gemert, "Light scattering in Intralipid–10% in the wavelength range of 400-1100 nm," Appl. Opt. **30**, 4507–4514, (1991).
27. W. Xia, D. Piras, M. Heijblom, W. Steenbergen, T. G. van Leeuwen and S. Manohar, "Poly(vinyl alcohol) gels as photoacoustic breast phantoms revisited," J. Biomed. Opt. **16**(7), 075002, (2011).
28. J. A. Curcio and C. C. Petty, "The near infrared absorption spectrum of liquid water", J. Acoust. Soc. Am. **41**(5), (1951), 302–304
29. F. Martelli and G. Zaccanti "Calibration of scattering and absorption properties of a liquid diffusive medium at NIR wavelengths. CW method," Opt. Express **15**(2), 486–500, (2007).

#194418 - $15.00 USD Received 25 Jul 2013; revised 10 Sep 2013; accepted 13 Sep 2013; published 23 Oct 2013

30. L. Spinelli, A. Torricelli, A. Pifferi, P. Taroni, G. M. Danesini, and R. Cubeddu "Bulk optical properties and tissue components in the famale breast from multiwavelength time-resolved optical mammography" J. Biomed. Opt. **9**(6), 1137–1142, (2004).
31. A. Roggan, M. Friebel, K. Dorschel, A. Hahn and G. Muller "Optical properties of circulating human blood in the wavelength range 400-2500 nm," J. Biomed. Opt. **4**(1), 36–46, (1999).
32. B.T. Cox and P.C. Beard, "Fast calculation of pulsed photoacoustic field in fluids using k-space metholds," J. Acoust. Soc. Am. **117(6)**, 3616–3627, (2005)
33. B. E. Treeby, and B. Cox, "k-Wave: MATLAB toolbox for the simulation and reconstruction of photoacoustic wave fields," J. Biomed. Opt. **51**(2), 021314, (2010)
34. B. E. Treeby, E. Z. Zhang and B. Cox, "Photoacoustic tomography in absorbing acoustic media using time reversal," Inverse Problems **26**, 115003, (2010)
35. J. Folkman, "Tumor angiogenesis," in *Cancer Medicine*, J. F. Holland, Ed., 5th ed. (Hamilton, ON: B. C. Decker, 2000), ch. 9, pp. 132152.
36. G. Bergers and L. E. Benjamin, "Tumorigenesis and the angiogenic switch," Nat. Rev. Cancer. **3**, 401–410 (2003). (doi: 10.1038/nrc1093)
37. S. Huang, J. M. Boone, K. Yang, N. J. Packard, S. E. McKenney, N. D. Prionas, K. K. Lindfors and M. J. Yaffe, "The characterization of breast anatomical metrics using dedicated breast CT," Med. Phys. **38**(4), 2180–2190 (2011).
38. ANSI, Z136.1-2007.
39. S. A. Ermilov, A. Conjusteau, T. Hernandez, R. Su, V. Nadvoretsky, D. Tsyboulski, F. Anis, M. A. Anastasio, and A. A. Oraevsky, "3D laser optoacoustic ultrasonic imaging system for preclinical research," Proc. SPIE 8581, 85810N, (2013).
40. J. Jose, R. G. H. Willemink, S. Resink, D. Piras, J. C. G. van Hespen, C. H. Slump, W. Steenbergen, T. G. van Leeuwen and S. Manohar, "Passive element enriched photoacoustic computed tomography (PER PACT) for simultaneous imaging of acoustic propagation properties and light absorption," Opt. Express **19**(3) 2093–2104 (2011).
41. C. Li, N. Duric, P. Littrup, and L. Huang, "In vivo breast sound-speed imaging with ultrasound tomography," Ultrasound Med. Biol. **35** 1615–1628 (2009).

1. Introduction

Breast cancer is the leading cause of cancer death in females worldwide [1]. Early detection increases survival rate [2]. X-ray mammography, ultrasonography and magnetic resonance imaging (MRI) are the commonly used imaging modalities for breast cancer detection and diagnosis. All of these techniques have their limitations: X-ray mammography besides possessing ionizing hazards, is less sensitive in women with dense breasts [3]. Ultrasonography in breast imaging suffers from poor soft tissue contrast [3], operator dependence, and lack of standardization. MRI has high sensitivity but suffers from a limited specificity, a relatively high cost and requires the use of a contrast agent [3]. Since many of these limitations are related to the fundamental nature of the techniques, there is a great need for an alternative breast imaging modality to detect and diagnose early stages of cancer with high sensitivity and specificity.

Owing to the high and spectroscopically rich optical contrast shown by cancer, optical mammography can potentially solve the problems of the conventional imaging modalities, which in addition to the above mentioned drawbacks focus primarily on morphological changes. However, the method suffers from poor resolution due to strong light scattering in biological tissue [4]. Photoacoustic (PA) imaging addresses this limitation by allowing the absorbing chromophores to emit ultrasound (US) waves in response to short pulsed laser light excitation by thermo-elastic expansion. The US waves arrive at the detection site at the tissue surface with less losses and scattering than light in optical mammography. Marrying light and sound, PA imaging on the one hand takes the advantages of optical imaging, offering vascularization-driven optical absorption tumor contrast, and on the other, the advantages of ultrasound imaging, offering a superior ultrasound resolution with a large imaging depth [5–7]. The method holds tremendous promise to detect angiogenic markers of breast cancer based on hemoglobin absorption [8–15].

Several photoacoustic (thermoacoustic) dedicated breast imaging systems have been reported

#194418 - $15.00 USD Received 25 Jul 2013; revised 10 Sep 2013; accepted 13 Sep 2013; published 23 Oct 2013

in the past decade [8–10, 12, 13, 15]. The group of Oraevsky developed a semi-circular laser optoacoustic imaging system (LOIS) which has undergone several iterations [10, 16]. The detection is based on an arc-shaped array of 64/32 polyvinylidene fluoride (PVDF) detector elements, with a 1 MHz center frequency and an ultra-broad bandwidth (upto 2.5 MHz). Two excitation wavelengths (1064 and 757 nm) have been employed [10, 17]. The latest system promises to faithfully recover deep embedded objects with sub-millimeter resolution [10]. However, the system design gives the detector a slice-shape focusing area, visualizing only a cross-sectional breast slice.

The group of Wang developed a circular breast imaging system combining photoacoustic (PAT) and thermoacoustic tomography (TAT) [13]. TAT is the microwave excited analog of photoacoustics, and potentially provides additional information of increased ionic water concentration associated with the neovascularization. TAT also has potentially a superior imaging depth compared to PAT, which has been previously demonstrated by the group of Kruger [18]. The Wang system excitation uses 0.5 μs, 3.0 GHz microwave and 6.5 ns, 1064 nm wavelength laser pulses. Ultrasound detection is with 13 mm/6 mm-diameter non-focused detectors with 2.25 MHz center frequency (ISS 2.25 x 0.5 COM, Krautkramer). Good quality PAT and TAT images on tissue phantoms have been achieved, however, the present system is still only capable of performing 2D slice imaging.

The group of Jiang recently demonstrated a hybrid PAT and diffuse optical tomography (DOT) system based on a circular detection geometry for breast imaging [15], which combined the high resolution possible with PAT with the spectroscopic functional information possible with DOT [4]. However, the system design only allows for 2D imaging.

These PA systems are promising for breast cancer imaging, but they suffer from poor cross-plane spatial resolution. The group of Kruger recently reported a 3D PAT system based on a hemispherical geometry, which overcomes the limitation of 2D imaging, providing an uniform spatial resolution [9]. The excitation uses 800 nm wavelength while US detection employs 128 detector elements, 3 mm in diameter with a 5 MHz center frequency, arrayed in a spiral pattern covering the inner surface of a hemispherical bowl. Breast vasculature down to a depth of 40 mm was successfully visualized with submillimeter resolution [9]. However, since US detection was initially optimized for small animal imaging, the authors recommend the use of a lower frequency detector for better sensitivity. Another limitation of the system is the limited field-of-view (FOV) (64 x 64 x 50 mm^3) for full breast imaging due to the narrow acceptance angle of the detector at high center frequency.

Our group has developed a planar geometry imager, the Twente Photoacoustic Mammoscope (PAM) [19]. The US detection is based on a 2D array of 590 PVDF detector elements, with a 2 x 2 mm surface area, a 1 MHz center frequency and a 130% fractional bandwidth. Light excitation uses 1064 nm wavelength. The system is capable of 3D imaging with 2.3-3.9 mm spatial resolution. We reported our first clinical experiences in 2007, where we showed that carcinoma could be visualized in 4 of the 5 cases studied [20]. Recent clinical results in 2012 corroborated the earlier studies, while showing the successful visualization of malignancies with a superior imaging contrast to X-ray mammography [14]. Further, the contrast of PAM was found to be independent of fibroglandular breast density. However, the system suffers from a small FOV (40 x 40 x 50 mm^3) and a relatively low sensitivity of the PVDF detector.

In this article we describe a new system which addresses many of the limitations of current breast imagers. This laboratory prototype is implemented in a cylindrical geometry using a linear US detector array optimized for ultra-high sensitivity [21], and permits 3D imaging to be performed. We present the system design with special attention to a new detector array and its characterization, such as frequency response, directional sensitivity, minimum detectable pressure (MDP) and inter-element cross-talk. We further evaluate the resulting performance of

#194418 - $15.00 USD Received 25 Jul 2013; revised 10 Sep 2013; accepted 13 Sep 2013; published 23 Oct 2013

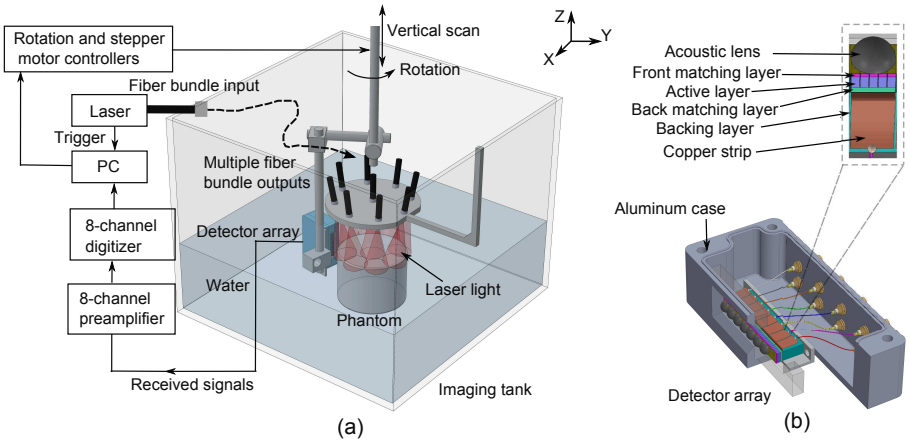

Fig. 1. Schematics of (a) the PAM-II laboratory prototype system and (b) the linear array detector.

the imaging system in terms of spatial resolution, sensitivity, imaging quality and FOV using well characterized tissue phantoms. We finally discuss the various recommendations to guide this laboratory prototype system towards a clinical version, which will be the second generation Twente Photoacoustic Mammoscope (PAM-II).

2. Materials and methods

2.1. The system

2.1.1. Light source and light delivery system

The schematic of the new laboratory prototype system is shown in Fig. 1(a). A laser system combining a Q-switched Alexandrite and a Q-switched Nd:YAG is used for NIR light excitation (QCombo, Quanta System, Milan, Italy). The laser emits 60-ns pulses at 755 nm and 5-ns pulses at 1064 nm with a 10 Hz repetition rate for both wavelengths. The maximum output pulse energy for both wavelengths is around 300 mJ, which can be reduced using motorized attenuators. The laser pulses at both wavelengths share the same optical path reaching the output of the unit. The laser is operated either in a single-wavelength mode (755 nm or 1064 nm) with a 10 Hz repetition rate or in a double-wavelength mode interleaving the two wavelengths with a 20 Hz repetition rate. Other light sources were also considered, such as dye lasers and Ti: Sapphire lasers, which have a wider wavelength tuning compared to the dual-head laser used. However, theses lasers were not chosen predominantly due to their insufficient pulse energies.

The output laser beam is coupled into a fiber bundle (1 input : 9 outputs) and illuminates the breast phantom as shown in Fig. 1(a). In a clinical version of the instrument, the patient will lie in a prone position as in Ref. [9], with her breast pendant. In this case illumination will be from the bottom on the nipple. The input diameter of the fiber bundle is 9 mm, and each of the output has a diameter of 3.5 mm (LGO Optics, San Jose, CA). The laser beam is naturally spread out from each output to cover the entire breast (or breast phantom) surface. The maximum output laser energy that can be delivered from each fiber output is around 9 mJ.

The 1064 nm wavelength is selected for the large optical penetration depth in breast tissue [22]. At this wavelength, in addition to absorption by predominantly oxy-hemoglobin, the contributions to PA signals from water, lipid and collagen may be non-negligible. Thus a second wavelength at 755 nm is chosen where the absorption by water and lipid is low, with deoxy-hemoglobin having a local peak [10, 17, 23]. However, only 755 nm wavelength is used in this

#194418 - $15.00 USD Received 25 Jul 2013; revised 10 Sep 2013; accepted 13 Sep 2013; published 23 Oct 2013

work for phantom experiments.

2.1.2. Ultrasound detector array

An 8-element linear array prototype detector is used for US detection. The detector array is based on the design of a single-element detector optimized for high sensitivity for PAT of the breast. The detailed description of the design and development of this single-element detector is presented in Ref. [21], and shown in Fig. 1(b). Briefly, the detector center frequency is chosen to be around 0.6 MHz with a 75% bandwidth based on the requirement to detect tumors larger than 2 mm. We begin with a PZT material of thickness 1.625 mm providing a resonant frequency of 1.2 MHz [21], which undergoes a spectral shift with the addition of matching layers and an acoustic lens to 0.6 MHz [21, 24]. Together with a surface area of 5x5 mm the high PZT thickness ensures a high sensitivity for ultrasound detection. Thus, each single-element of the detector array is made of highly sensitive active PZT material of 1.625 mm thickness (CTS 3203HD, CTS Communications Components, Inc., Albuquerque, NM), a front matching layer (0.7 mm thickness, electrical conductive epoxy), a back matching layer (0.48 mm thickness, electrical conductive epoxy) and a backing layer (10 mm thickness) with a 5 x 5 mm surface area. Each detection element is sub-diced by cutting 0.1 mm air kerfs to reduce radial resonances caused by the large thickness/width ratio of the active material. With sub-dicing through the front matching layer and active material, an element is subdivided into 25 small units with dimensions of 0.9 x 0.9 mm (Fig. 1(b)). Thus the sub-units are separated acoustically by the air kerfs while being grouped electrically by an aluminium foil (see further).

For fabricating the detector array (Fig. 1(b)), a block of the PZT material of dimensions 40 x 5 x 1.625 mm is first diced into individual elements with a 0.15 mm air kerf cutting through the front matching layer into the backing layer. The center-center distance of each element is 5 mm. A layer of thin aluminum foil is epoxied on top of the front matching layer and is used as the electrical grounding. To protect the aluminum foil, a thin kapton foil layer is glued on top. The signal for each element is taken from a copper strip connected to the electrical conductive back matching layer. A 5 mm diameter hemispherical acoustic lens made of Stycast 1090SI (Henkel, Düsseldorf, Germany) possessing well-suited acoustic properties is attached on top of each element to enlarge the acceptance angle of the detector for full breast imaging [24]. The detector array is fixed inside an aluminum case with a rectangular aperture with the same dimensions as the detector array. The surface of the detector array through the aperture is flush with the aperture of the aluminum box to have complete electromagnetic shielding.

The detector array is situated at a distance of 11 cm from the center of the phantom and rotated around it to acquire projections with top-illumination (Fig. 1(a)). The detector array is scanned along vertical direction to acquire multiple sets of projections to compensate for the large center-center distance between elements (5 mm).

2.1.3. Data acquisition

The PA signals detected by the detector array are amplified by an 8-channel prototype low noise preamplifier based on ADA4896-2 (Analog Devices, Norwood, MA) with a $\sim$20 dB gain as the analog front-end and acquired using a high-speed 8-channel digitizer (NI PXI-5105, 60 MS/s, 12-Bit, National Instruments, Austin, TX) and saved for data processing.

2.1.4. Detector frequency response

The frequency response of a typical single detector element (element 5) in the array is measured in pulse-echo mode (Fig. 2(a)), based on the validity of the reciprocity principle for the piezoelectric material [25]. The detector element is driven by a broadband ultrasonic pulser/receiver (Panametrics 5077PR). The transmitted US pulse is reflected by a stainless steel plate situated

#194418 - $15.00 USD Received 25 Jul 2013; revised 10 Sep 2013; accepted 13 Sep 2013; published 23 Oct 2013

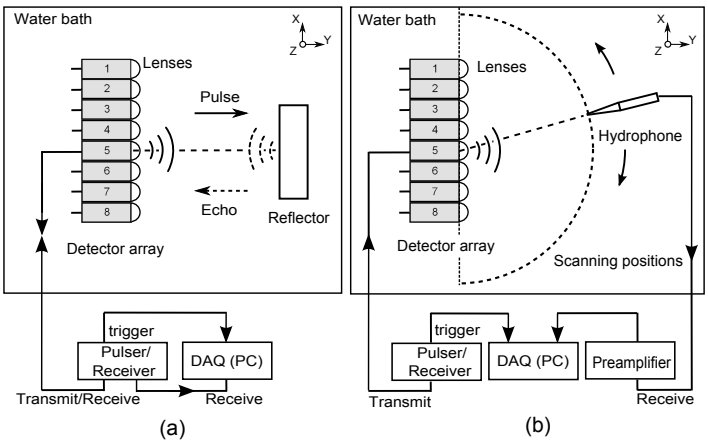

Fig. 2. Schematics of measurement setups used for studying (a) pulse-echo and frequency responses and (b) directional sensitivity.

in the far-field ($\sim$55 mm away) perpendicular to the detector element . The pulse-echo signal is received by the same detector element using a data acquisition (DAQ) card (U1067A Acqiris, 8 bit, 500 MS/s). The frequency response of the detector is calculated by the square root of the FFT of the measured pulse-echo signal to account for the two-way response.

2.1.5. Detector directional sensitivity

The directivity of the detector element 5 is measured in transmit mode (Fig. 2(b)). The detector array is mounted in a demineralized water bath at room temperature. The detector element is driven by the ultrasonic pulser/receiver (Panametrics 5077PR) as a transmitter. A calibrated needle hydrophone (BLLMCX074 Precision Acoustics Ltd. Dorchester) is rotated in the far-field centered on the detector element to probe the emitted US field in the plane covering 180^o in steps of 1^o (Fig. 2(b)). The acoustic signals are acquired using a DAQ card (U1067A Acqiris, 8 bit, 500 MS/s). For each scanning position, the peak-to-peak value of the received US pulse is noted and plotted as a function of the scanning angle, giving the directional sensitivity of the detector element at its center frequency.

2.1.6. Detector sensitivity and minimum detectable pressure

To ascertain sensitivity and minimum detectable pressure (MDP) of the detector elements one at a time, a substitution method is used. A 0.5 MHz focused Panametrics broadband transducer is used as a transmitter driven by a 100 cycles sine wave at 0.6 MHz (the central frequency of the detector, see Results Sec. 3.1 and Fig. 4(b)) to pinpoint and insonify one detector element of the array along its acoustic axis. Progressively reducing pressures are applied by lowering the input voltage to the transmitter till the lowest input possible. Signals from the detector element under investigation after 100 averages and amplification by the 8-channel prototype low noise preamplifier are recorded by the 8-channel digitizer. The root mean square (RMS) value of the signals are calculated and defined as measured voltages. Next the calibrated needle hydrophone is used to measure the pressures from the US transmitter in separate measurements. Finally, the electrical noise (no average) is measured separately when the detector has no driving signal, and its RMS value is calculated. The measured voltages are plotted against pressure inputs and the trend (linear fit) is extended to intersect the voltage noise floor (noise RMS). The slope of the trend gives the sensitivity, and the pressure at the intersection point of the trend with noise

#194418 - $15.00 USD Received 25 Jul 2013; revised 10 Sep 2013; accepted 13 Sep 2013; published 23 Oct 2013

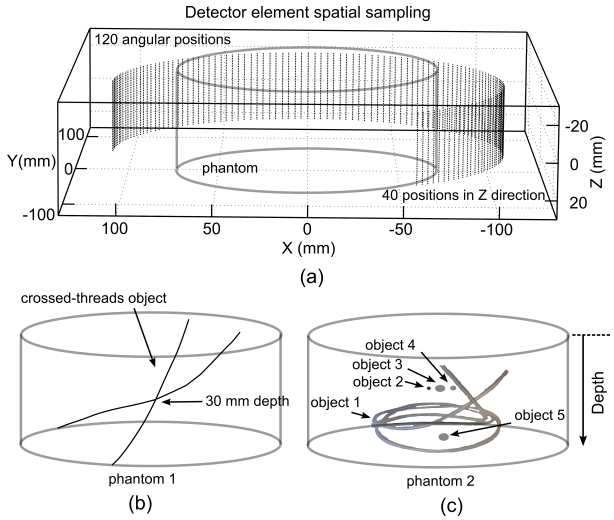

Fig. 3. (a) Schematic of the tomographic system showing the relative positions between the scanning detector element and the phantom. (b) Schematic of phantom 1: a crossed-threads object embedded in Agar/Intralipid gel cylinder. (c) Schematic of phantom 2: five objects embedded in Agar/Intralipid gel cylinder. Detailed descriptions of the phantom and object properties are listed in Table 1. The lower part of the phantom is not shown in all three schematics.

level is the MDP (or noise equivalent pressure) at the detector center frequency (0.6 MHz).

The measurement procedure is repeated for each detector element, giving the end-of-cable sensitivity and MDP for the US detection system chain including the US detector, the preamplifier and the digitizer.

2.1.7. Detector inter-element electrical and mechanical crosstalk

The levels of electrical and acoustic isolation between detector elements are measured in a demineralized water bath by driving element 5 with a 1 cycle sine burst at the detector center frequency (0.6 MHz) with a peak-peak amplitude of 5 V. The responses of all elements are directly sent to the 8-channel digitizer. The electrical leakage (electrical crosstalk) from the driven element to the rest of the elements can be recognized by the lack of phase-shift relative to the driven signal. On the other hand, the mechanical crosstalk has a time delay relative to the driving signal depending on the distance from the element of interest to the active element.

2.2. Phantom experiments

2.2.1. Detector scanning procedure

The detector array is oriented in vertical direction situated at a distance of 11 cm from the rotation center to scan the phantom covering 240^o in steps of 2^o to acquire PA signals (100 averages) as shown in Fig. 3(a). A complete circular scan could not be performed due to mechanical constraints (holder for the detector). When this rotational scan is complete, the detector is moved back to the original position and then moved 1 mm lower to perform another rotational scan. Five such rotational scans are performed to increase the density of the detector spatial sampling in vertical direction (Fig. 3(a)). The total number of detection positions can then be calculated as 8 x 5 x 120 = 4800. A full volume scan in the laboratory prototype takes around 1 hour.

#194418 - $15.00 USD Received 25 Jul 2013; revised 10 Sep 2013; accepted 13 Sep 2013; published 23 Oct 2013

Table 1. Background and object properties of phantom 2. Their dimensions, distances from phantom surface (depths), optical reduced scattering coefficient μ_s', and optical absorption coefficient μ_a are listed. The optical properties of normal and cancerous breast tissue are derived from Ref. [30] at 755 nm and human blood is derived from Ref. [31] at 800 nm, where blood absorption is independent of the oxygen saturation level.

	dimensions	depth (mm)	μ_s' (mm^{-1})	μ_a (mm^{-1})	equivalent to
background	diameter 130 mm	-	0.7	0.003	normal breast tissue[a]
object 1	tube inner diameter 1 mm	5-40	0.7	0.1	blood vessel[b]
object 2	2 mm sphere	20	0.7	0.1	blood vessel[b]
object 3	10 mm sphere	20	0.7	0.01	tumor[a]
object 4	5 mm sphere	20	0.7	0.01	tumor[a]
object 5	10 mm sphere	40	0.7	0.01	tumor[a]

[a] Ref. [30].
[b] Ref. [31].

2.2.2. Phantoms

Two phantom experiments are performed. Phantom 1 is used to study the system resolution and FOV. Two red nylon fishing threads (0.28 mm diameter) are crossed in the middle and embedded in a Agar/Intralipid gel phantom (2% agar in weight, Sigma-Aldrich, Germany, and 0.3% Intralipid in volume, batch no. WI15893, Fresnius Kabi Nederland BV, The Netherlands) with an optical reduced scattering coefficient $\mu_s' = 0.35\ mm^{-1}$ [26,27], and an optical absorption coefficient $\mu_a = 0.003\ mm^{-1}$ [28, 29] at 755 nm wavelength. The phantom has a cylindrical shape with a diameter of $\sim$130 mm and with a height of $\sim$120 mm. The fishing threads are embedded in the upper part of the cylinder and span over $\sim$60 mm depth as shown in Fig. 3(b). The phantom is mounted on a heavy metal plate to stabilize the phantom at the bottom of the imaging tank. The PA signals and acoustic reflections from the metal plate are well separated from the PA signals from the object.

Phantom 2 is used to study the sensitivity of the system. The phantom background has the similar design used for phantom 1 only with higher Intralipid concentration (0.6% Intralipid in volume) to mimick μ_s' and μ_a of normal breast tissue at 755 nm [30]. Various inhomogeneities are embedded in the phantom. Object 1 is a soft plastic tube (1 mm inner diameter, LsmaTec, Glattbrugg, Switzerland) filled with Agar gel formed in an aqueous dilution of Intralipid and Indian ink (Royal Talens, the Netherlands) for $\mu_a = 0.1\ mm^{-1}$. The tube is arranged in a spiral pattern spanning over 40 mm depth. Objects 2 to 5 comprise four spherical objects made of the same Agar gel, embedded at different depths inside the phantom (Fig. 3(c)). These objects have various diameters (Table 1), and optical absorptions (object 2 has $\mu_a = 0.1\ mm^{-1}$, objects 3-5 have $\mu_a = 0.01\ mm^{-1}$). The detailed description of the object location, dimensions, and their optical properties are listed in Table 1. The spherical objects are made of Agar/Intralipid as for the phantom background, with an additional Indian ink dilution.

The ink dilutions above are obtained from a stock solution of 1% v/v ink in water. The μ_a of the stock is measured using a spectrophotometer (Shimadzu UV-3101 PC, Tokyo, Japan) and found to possess a μ_a of $0.25\ mm^{-1}$ at 755 nm. The stock solution is then diluted to give appropriate absorptions for the objects to mimic either tumor tissue (0.04% v/v Indian ink in water, $\mu_a = 0.01\ mm^{-1}$) or human blood aborption (0.4% v/v Indian ink in water, $\mu_a = 0.1\ mm^{-1}$) [30, 31].

#194418 - $15.00 USD Received 25 Jul 2013; revised 10 Sep 2013; accepted 13 Sep 2013; published 23 Oct 2013

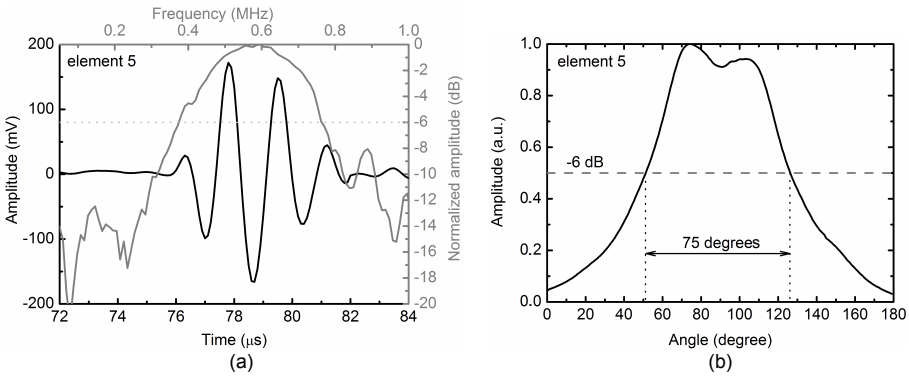

Fig. 4. (a) Pulse-echo and frequency response, and (b) directional sensitivity of the detector element 5.

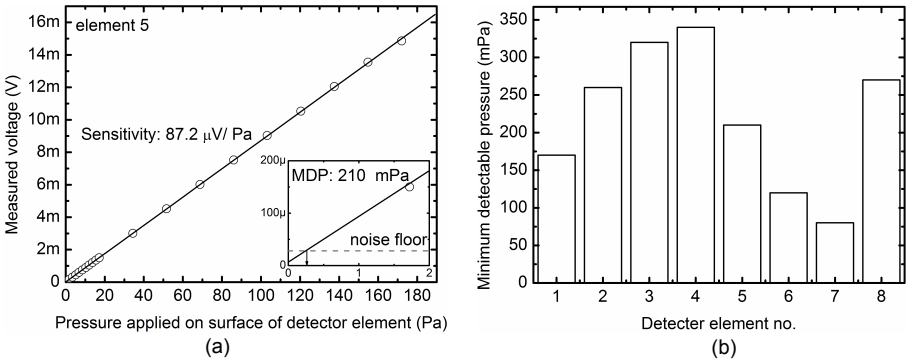

Fig. 5. (a) Sensitivity and minimum detectable pressure of the detector element 5. (b) Minimum detectable pressure for each element in the detector array.

2.2.3. Image reconstruction

The PA signals after filtering (3rd order Butterworth bandpass filter with 0.15 and 1.5 MHz cutoff frequency) are fed into the k-Wave package for image reconstruction using time-reversal [32–34]. The images are reconstructed by back-propagating the received signals in time reversed order, as a Dirichlet boundary condition over defined sensor positions in 3D. A single speed of sound (SOS) value is assigned to the entire acoustic domain. The SOS value is optimized during reconstruction iteration to be 1495 m/s for the best image quality. The images are reconstructed with a 0.5 x 0.5 x 0.5 mm^3 voxel size and interpolated for better visualization.

3. Results

3.1. Detector array performance

Figure 4(a) shows the measured pulse-echo and frequency response of element 5. The element with acoustic lens has a center frequency and fractional bandwidth of 0.6 MHz and ∼75%, respectively. The measured directional sensitivity of the element 5 is shown in Fig. 4(b). The directivity angle is enlarged to be around 75º by the acoustic lens, which is sufficient for full breast imaging.

The measured sensitivity and MDP for element 5 are 87.2 μV/Pa and 210 mPa as shown in Fig. 5(a). MDP variations in all elements in the array are shown in Fig. 5(b). The mean ± stan-

#194418 - $15.00 USD Received 25 Jul 2013; revised 10 Sep 2013; accepted 13 Sep 2013; published 23 Oct 2013

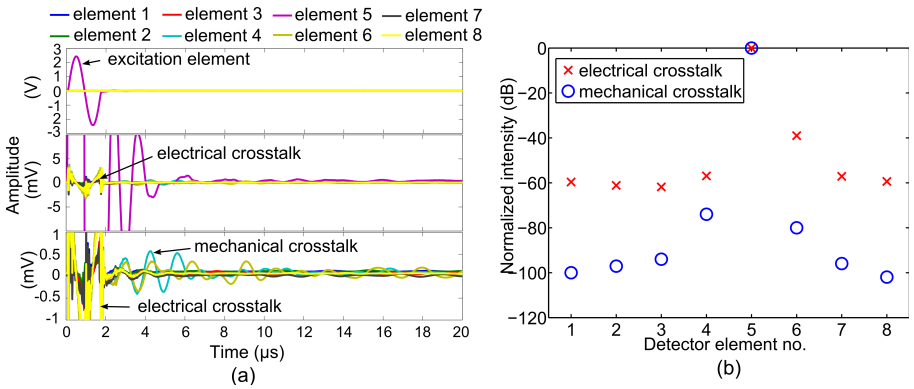

Fig. 6. (a) Responses of all elements in the array displayed in different vertical scales for visualization. Electrical and mechanical crosstalk are well separated in time. (b) Peak-peak inter-element electrical and mechanical crosstalk of the linear array detector relative to the driven element.

dard deviation MDP of the array is 221 $\pm$ 93 mPa. To our knowledge, this is the lowest reported MDP measured for a detector in photoacoustic breast imaging. The MDP variations are large and mainly due to the noise variations present for the DAQ channels. The measured MDP using this method takes the full noise frequency spectrum into account. However, in practice, when signal de-noising is applied, the MDP value can be reduced.

The results of inter-element electrical and mechanical crosstalk are shown in Fig. 6 with the responses of all elements in Fig. 6(a). The responses are plotted in three grouped subplots with different Y-axis units for better visualization. The strong excitation signal for element 5 can be clearly seen from the upper plot, while the responses from the other elements are not visible. The electrical and mechanical crosstalk can be identified from two zoom-in plots at middle and bottom. The peak to peak voltage of the measured electrical and mechanical crosstalk for all the elements are compared to the driving element response in Fig. 6(b). A low mechanical crosstalk level can be observed which is possibly due to the additional air kerf separation between the sub-diced small units for each element.

3.2. Spatial resolution of the system

Phantom 1 is dedicated for the system resolution study. A top view maximum intensity projection (MIP) image of the phantom extracted from the 3D reconstruction is shown in Fig. 7(a). The image has a 100 x 100 mm^2 FOV. A side view MIP of the phantom is shown in Fig. 7(b) with a 60 x 100 mm^2 FOV. The crossed-threads object is successfully visualized. Two MIP movies showing the rotation of the 3D object can be viewed in Media 1 and Media 2. A 3D rendering of the phantom with a 110 x 110 x 70 cm^3 FOV is shown in Fig. 7(d).

We analyzed the spatial resolution of the system in the XY plane (axial and lateral) and Z direction (vertical). A image slice at the location indicated by a white dashed line in Fig. 7(a) is taken from the 3D reconstruction. This is depicted in Fig. 7(c) showing cross-sections of the two threads at around 40 mm from the phantom surface. Axial and lateral profiles are taken from the thread cross-sections indicated by dashed lines in Fig. 7(c), and shown in Fig. 7(e) and (f) for cross-section “1”, and (g) and (h) for cross-section “2”, respectively. The full width at half maximum values of axial and lateral profiles indicate that the system has a 2 mm spatial resolution in the XY plane and 6 mm in Z direction at locations around 40 mm from phantom surface.

#194418 - $15.00 USD Received 25 Jul 2013; revised 10 Sep 2013; accepted 13 Sep 2013; published 23 Oct 2013

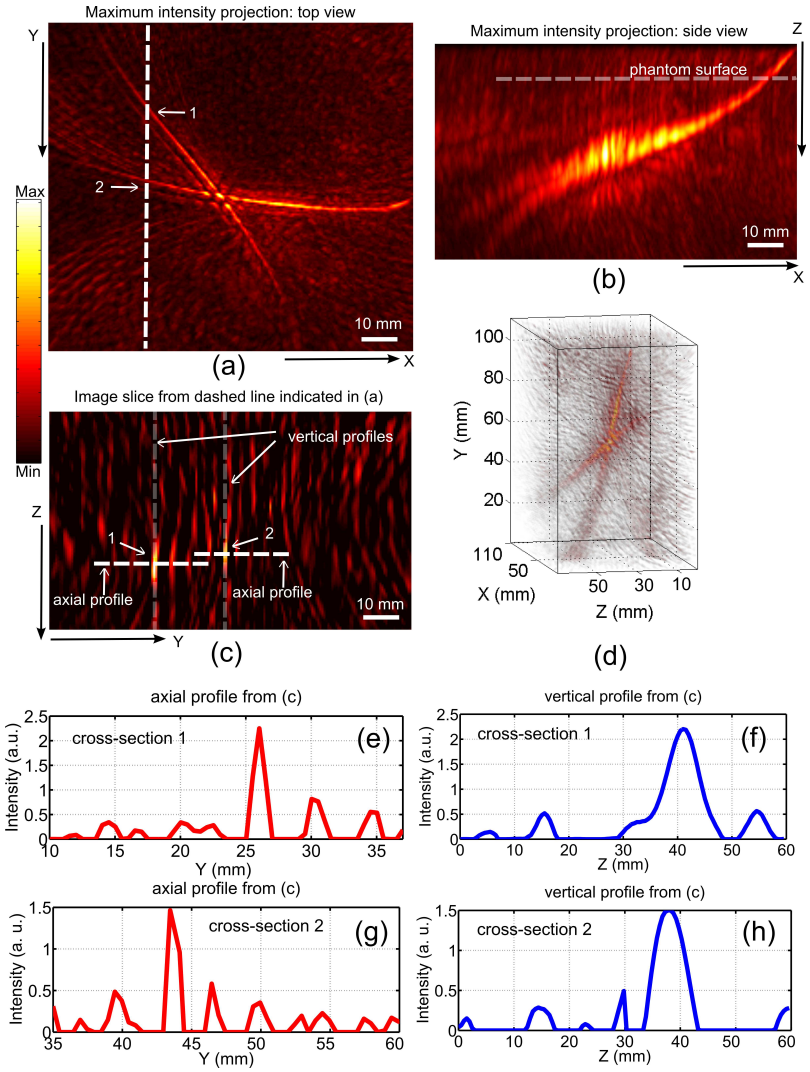

Fig. 7. Reconstruction of phantom 1. (a) A top view maximum intensity projection (MIP) along the vertical axis (Z direction) with 100 x 100 mm^2 field of view. (b) A side view MIP along the Y direction with 60 x 100 mm^2 field of view. Two MIP movies showing the rotation of the 3D phantom around two orthogonal axes can be viewed in Media 1 and Media 2 respectively. (c) An image slice at position indicated by dashed line in (a) showing cross-sections of the two threads (marked with "1", and "2") at around 4 cm from the phantom surface. (d) A 3D rendering of the phantom showing a 110 x 110 x 70 mm^3 field of view. (e) An axial profile crossing a sub-resolution object ("1") from (c) indicated by a dashed white line, and (f) A vertical profile crossing a sub-resolution object ("1") from (c) indicated by a dashed gray line. (g) An axial profile crossing a sub-resolution object ("2") from (c) indicated by a dashed white line, and (h) A vertical profile crossing a sub-resolution object ("2") from (c) indicated by a dashed gray line.

#194418 - $15.00 USD Received 25 Jul 2013; revised 10 Sep 2013; accepted 13 Sep 2013; published 23 Oct 2013

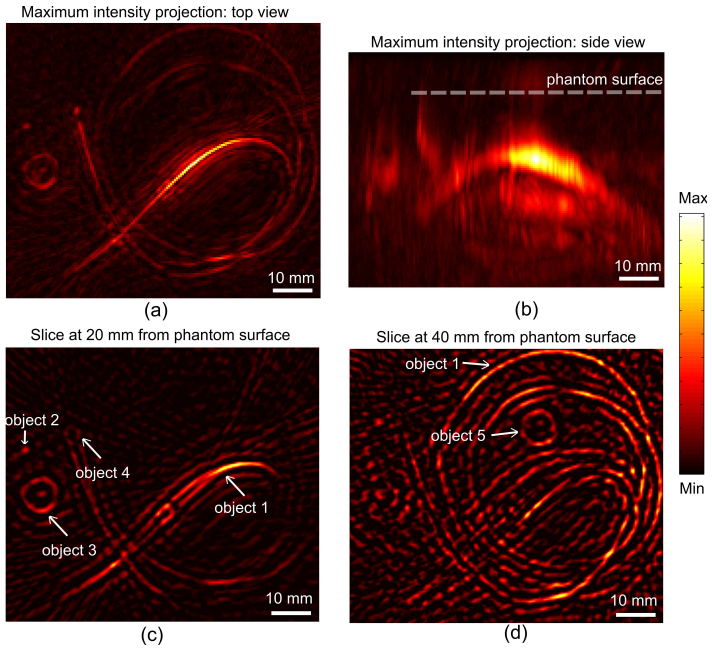

Fig. 8. Reconstruction of phantom 2. (a) A top view maximum intensity projection (MIP) along the vertical axis (Z direction) with 70 x 70 mm^2 field of view. (b) A side view MIP along the X direction with 60 x 70 mm^2 field of view. Two MIP movies showing the rotation of the 3D phantom around two orthogonal axes can be viewed in Media 3 and Media 4 respectively. (c) A XY plane image slice at 20 mm depth from the phantom surface showing the reconstructed objects on this plane. (d) A XY plane image slice at 40 mm depth from the phantom surface showing the reconstructed objects on this plane.

3.3. Sensitivity and imaging quality of the system

Phantom 2 possesses a background $\mu_s' = 0.7\ mm^{-1}$ to mimic normal breast tissue scattering, and objects with different sizes possessing μ_a for either tumor tissue or blood vessel absorption located at various depths. This phantom was designed to evaluate the sensitivity and imaging quality of the system. A top view and a side view MIP image of the phantom are shown in Fig. 8(a) and (b), respectively. Two MIP movies showing the rotation of the 3D phantom can be viewed in Media 3 and Media 4. Figure 8(c) and (d) are the XY plane image slices at 20 and 40 mm depth from the phantom surface. All objects are successfully visualized including a blood vessel mimicking object (object 1) down to a depth of 40 mm, a 2-mm-diameter spherical object with blood absorption (object 2) at 20 mm depth, a 5-mm-diameter tumor mimicking spherical object (object 4) at 20 mm depth, and two 10-mm-diameter tumor mimicking objects (objects 3 and 5) at 20 and 40 mm depths. Details of the background and object optical properties, object size, location are listed in Table 1.

3.4. Field-of-view of the system

Figure 7(d) shows a 110 x 110 x 70 mm^3 FOV of the 3D reconstructed phantom 1. Even larger -6 dB FOV of around 170 x 170 x 170 mm^3 can be estimated from the -6 dB acceptance angle of the detector element (75°, Fig. 4(b)).

#194418 - $15.00 USD Received 25 Jul 2013; revised 10 Sep 2013; accepted 13 Sep 2013; published 23 Oct 2013

4. Discussion

We presented the design and evaluated the performance of a laboratory prototype system for photoacoustic breast tomography. The detector characterization shows that the detector array possesses a mean MDP of 221 mPa, which is lower than our previously reported value (500 mPa) [21]. This is due to the improved electrical grounding and shielding of the detector. The detector has a 0.6 MHz center frequency with a 75% fractional bandwidth. The implications and suitability of the relatively narrow bandwidth are discussed further. The acceptance angle of the detector is enlarged by the lenses to be around 75^{o} at the detector center frequency. The large acceptance angle of the detector ensures a large FOV of the system.

The imaging performance of the system was evaluated using phantom experiments. The resulting 2 mm XY plane resolution determined by the bandwidth of the detector is sufficient for breast imaging. PA breast imaging is based on the tissue optical contrast due to vascularization, which is enhanced around a tumor due to angiogenesis [35]. This process is reported to go through two phases separated by the "angiogenic switch". Exponential tumor growth ensues in the second phase (vascular phase), which occurs from tumor sizes of 1-2 mm in diameter [36]. The 6 mm resolution in the Z direction (vertical resolution) is poor. This is due to the limited detector coverage of the phantoms in this direction. We cover only 45 mm of the 120 mm high phantom, due to the 5 scanning steps of the 40 mm long detector array. Further increasing the detector coverage in Z direction (see further Sec. 4.2) will improve the vertical resolution towards the bandwidth-determined 2 mm resolution.

Though image artifacts are present, a blood vessel mimicking object down to a 40 mm depth and a tumor mimicking object at 40 mm depth were successfully visualized, indicating a good sensitivity of the imager. Objects with 1-2 mm size (object 1 and 2) are faithfully recovered with well preserved shapes, while larger objects (object 3-5) are reconstructed with edge enhancement. This is due to the finite bandwidth of our detector (Fig. 4(a)), which does not cover the required low frequencies for PA signals generated from large objects. This observation matches the simulation results reported in Ref. [21]. The artifacts could be mitigated by deconvolution algorithms and iterative, model-based image reconstructions which will be implemented in the future. However, breast tumors are known to be heterogeneous with a scattered distribution of small absorbing regions, which makes our system well suited for sensitive clinical breast imaging due to the ultra-high sensitivity of the detector (Fig. 5) [21]. Further the bandwidth of the detector can be increased by using two or more front matching layers for future systems.

Our system FOV (170 x 170 x 170 mm^3) is considerably larger than that of Kruger's system (64 x 64 x 50 mm^3) [9]. As reported by Huang et al [37], the mean breast diameter and length for the bra cup size D was measured to be 137 mm and 97 mm, the FOV of our system is then suitable for 3D full breast imaging purpose.

A clinical version prototype system PAM-II will be developed based on the current system design. However, various design aspects can be further improved to address the above limitations.

4.1. Light delivery

The output laser energy delivered by the fiber bundle is around 80 mJ, which is spread out to cover a 13 cm diameter phantom surface, resulting in a 0.6 mJ cm^{-2} fluence at phantom surface. This intensity is far below the maximum permissible exposure for near infrared light [38].

However, 80 mJ is the maximum output energy that can be handled by the fiber bundle while the maximum energy from the laser output is around 300 mJ. For a future clinical version, a combination of fiber bundle and free-beam light delivery will be required. The latter could take the implementation of the Kruger system [9], where light falls on the pendant breast when patient lies prone from the nipple side. In such a case fiber bundle multiple outputs could be

#194418 - $15.00 USD Received 25 Jul 2013; revised 10 Sep 2013; accepted 13 Sep 2013; published 23 Oct 2013

appropriately distributed to provide illumination for the upper breast close to the chest line.

4.2. Ultrasound detection

The vertical resolution of the current system (6 mm) is limited by the curtailed Z direction coverage due to the use of a single array with limited Z direction scanning. For the clinical version, more detector arrays require to be stacked in the vertical direction in a detector arm. The detector arm can be arranged to curve along the contour of the pendant breast from chest wall to the nipple. With more detector elements in the vertical direction the Z axis resolution will be improved to that determined by the detection bandwidth, giving an isotropic spatial resolution of 2 mm.

Further, a multiple of such detector arms will be developed to be positioned around the breast. This will reduce the number of scanning positions around the breast. By this, the acquisition time of 1 hour for a full volume in the clinical prototype will be considerably reduced. Further, instead of the current 8 channel DAQ system, a 128 channel DAQ system under development will be used. A measuring time of under 10 minutes is aimed for.

4.3. Multi-modality imaging system

The experiments were performed using phantoms with SOS close to water. However, breast tissue in general has higher SOS than the coupling water, and with a heterogeneous distribution. For an accurate PA reconstruction, knowledge of SOS distribution in the breast is required. This can be obtained in future versions of the instrument using either ultrasound transmitters for SOS tomography, or using laser induced ultrasound to perform the same as adopted by Oraevsky et al [39] and Jose et al [40]. By these methods co-registration of SOS, acoustic attenuation (AA) and optical absorption can be performed. Further SOS and AA imaging can have diagnostic value since malignancies possess higher SOS and AA values compared with healthy tissues [41].

5. Conclusions

We presented the design and evaluation of a laboratory prototype system for 3D full breast imaging. The system is based on an optimized sensitive ultrasound detector array comprising 8 elements specifically developed for this purpose. Acoustic lenses are used to enlarge the acceptance angle of each large surface area element to ensure a wide system field of view. We characterized the detector array performance in terms of frequency response, directional sensitivity, minimum detectable pressure and inter-element electrical and mechanical cross-talk. We evaluated the performance of this laboratory prototype system using well-defined tissue mimicking phantoms. The system has a 2 mm XY plane resolution and a 6 mm vertical resolution. A vasculature mimicking object was successfully visualized down to a depth of 40 mm in a breast phantom. Further, tumor mimicking spherical objects with 5 and 10 mm diameter at 20 mm and 40 mm depths were recovered, indicating a good sensitivity of the system. The large acceptance angle of the detector ensures a 170 x 170 x 170 mm^3 system field of view, which is well suited for photoacoustic full breast tomography. With simple modifications within a patient-instrument interface this laboratory prototype can be developed into a clinical version with an isotropic spatial resolution of 2 mm.

Acknowledgments

The financial support of the Agentschap NL Innovation–Oriented Research Programmes Photonic Devices under the HYMPACT Project(IPD083374) and High Tech Health Farm, the Province Overijssel are gratefully acknowledged.